JACS
JOURNAL OF THE AMERICAN CHEMICAL SOCIETY

Article

pubs.acs.org/JACS

Site-Specific Growth of Au–Pd Alloy Horns on Au Nanorods: A Platform for Highly Sensitive Monitoring of Catalytic Reactions by Surface Enhancement Raman Spectroscopy

Jianfeng Huang,[†,§] Yihan Zhu,[†,§] Ming Lin,[‡] Qingxiao Wang,[⊥] Lan Zhao,[⊥] Yang Yang,[⊥] Ke Xin Yao,[†] and Yu Han*[,†]

[†]Advanced Membranes and Porous Materials Center, Physical Sciences and Engineering Division, and [⊥]Imaging and Characterization Core Lab, King Abdullah University of Science and Technology, Thuwal 23955-6900, Saudi Arabia

[‡]Institute of Materials Research and Engineering, A*STAR (Agency for Science, Technology and Research), 3 Research Link, Singapore 117602

Ⓦ *Web-Enhanced Feature* Ⓢ *Supporting Information*

ABSTRACT: Surface-enhanced Raman scattering (SERS) is a highly sensitive probe for molecular detection. The aim of this study was to develop an efficient platform for investigating the kinetics of catalytic reactions with SERS. To achieve this, we synthesized a novel Au–Pd bimetallic nanostructure (HIF-AuNR@AuPd) through site-specific epitaxial growth of Au–Pd alloy horns as catalytic sites at the ends of Au nanorods. Using high-resolution electron microscopy and tomography, we successfully reconstructed the complex three-dimensional morphology of HIF-AuNR@AuPd and identified that the horns are bound with high-index {11*l*} ($0.25 < l < 0.43$) facets. With an electron beam probe, we visualized the distribution of surface plasmon over the HIF-AuNR@AuPd nanorods, finding that strong longitudinal surface plasmon resonance concentrated at the rod ends. This unique crystal morphology led to the coupling of high catalytic activity with a strong SERS effect at the rod ends, making HIF-AuNR@AuPd an excellent bifunctional platform for *in situ* monitoring of surface catalytic reactions. Using the hydrogenation of 4-nitrothiophenol as a model reaction, we demonstrated that its first-order reaction kinetics could be accurately determined from this platform. Moreover, we clearly identified the superior catalytic activity of the rod ends relative to that of the rod bodies, owing to the different SERS activities at the two positions. In comparison with other reported Au–Pd bimetallic nanostructures, HIF-AuNR@AuPd offered both higher catalytic activity and greater detection sensitivity.

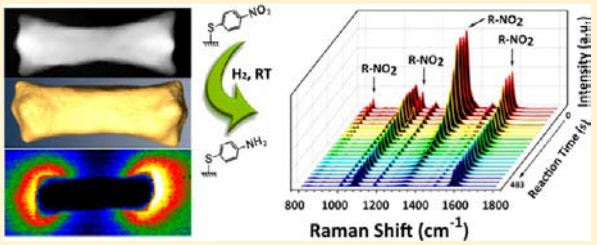

INTRODUCTION

In situ monitoring of a heterogeneous reaction on a catalyst surface is fundamentally crucial for understanding the reaction mechanisms and kinetics.[1] Conventional methods, such as Fourier transform infrared spectroscopy, mass spectroscopy, and gas chromatography, suffer from slow response, low sensitivity, or incapability to detect surface species and are therefore not able to reveal surface reactions in a real-time manner. In contrast, surface-enhanced Raman spectroscopy, which takes advantage of the plasmonic resonances in metallic nanostructures to obtain significantly enhanced Raman signals of the adsorbed molecules, allows fast-responsive and surface-selective detection with high sensitivity down to the single molecule level.[2]

Applying SERS to *in situ* monitoring of catalytic reactions requires developing an appropriate bifunctional platform that is both plasmonically and catalytically active. To this end, colloidal metallic nanocrystals (NCs) have been extensively investigated due to their localized surface plasmon resonance (SPR) effect, inherent activity for catalysis and compositional flexibility. Some core@shell bimetallic structures were developed, in which the performance (SERS or catalytic activity) of the core-metal was concealed by the shell component especially when the shell was compact and thick.[3] Better results were achieved in nanoparticles with hierarchical structures that were prepared by depositing one metal in the form of islands on a thin shell of another metal formed on top of an inner core (e.g., SiO_2@Au@Pd-islands by Wong et al.[1a] and Au@Pt@Au-islands by Schlucker et al.[1b]) to expose both plasmonic and catalytic sites. The obtained materials showed adequate catalytic and SERS-responsive functionalities and allowed catalysis to be probed via SERS. However, the complicated multistep preparation processes for these materials may result in inhomogeneous particle morphologies and hinder in-depth research on these systems as a consequence.

Integrating high SERS and catalytic activity into a simple and well-defined structure through facile synthesis, which requires a rational design that takes particle size, shape, composition, and nanoscale architecture into account, remains challenging.

Received: January 25, 2013
Published: May 15, 2013

dx.doi.org/10.1021/ja4004602 | *J. Am. Chem. Soc.* 2013, 135, 8552–8561

Metallic NCs with high-index facets usually show high catalytic activity owing to the high density of their low-coordinated atomic steps and kinks.[4] The synergetic effect between two metals often leads to enhanced catalytic activity for alloy NCs in comparison with their monometallic counterparts.[5] On the other hand, SERS activity is strongly dependent on the composition and shape of the NCs.[6] For example, gold and silver are the best candidates for SERS among various metals, and Au nanorods (AuNRs) with proper aspect ratios exhibit localized SPR concentrated on the rod ends, where the SERS effect is exceptionally strong.[7]

Here, we report the design and synthesis of a novel Au−Pd bimetallic nanostructure through selective growth of Au−Pd alloy horns on the ends of single-crystal AuNRs (denoted as HIF-AuNR@AuPd). We intentionally grew Au−Pd alloy rather than monometallic Pd on AuNRs for three reasons: (i) the Au−Pd alloy is more active than Pd alone in a large variety of catalytic reactions;[8] (ii) Au−Pd bimetallic NCs prepared via the seed-mediated coreduction[9] of metal ions tend to show exotic crystal morphologies with high-index facets (HIF) and thus superior catalytic activity;[4g] and (iii) in comparison with Pd, the Au−Pd alloy may have a smaller damping effect on the SPR of AuNRs, which allows them to maintain their SERS function.[10] Using high-resolution electron microscopy (HREM) and tomography, we successfully reconstructed the three-dimensional (3-D) morphology of the obtained material. The results showed that the Au−Pd alloy horns grew along the ⟨111⟩ direction with exposed high-index (approximately $\{11l\}$, $0.25 < l < 0.43$) side facets. Electron energy loss spectroscopy mapping conducted with HREM indicated the presence of intensive SPR on the two ends of the nanorods exactly where the horns were located. Such a configuration unites highly active catalytic sites with strong SERS sites in a single entity and is ideal for *in situ* monitoring of catalytic reactions by SERS. We successfully demonstrated this concept with a model reaction, i.e., the Pd-catalyzed hydrogenation of 4-nitrothiophenol (4-NTP) to 4-aminothiophenol (4-ATP), and found that HIF-AuNR@AuPd was superior to other Au−Pd nanostructures in both catalytic activity and SERS detection sensitivity. It is worth noting that such a bifunctional platform offers a unique opportunity to investigate the intrinsic reaction kinetics on the catalyst surface by excluding the influence of adsorption/desorption of reactants and products. In the model reaction, for example, the hydrogenation of a monolayer of 4-NTP molecules on the HIF-AuNR@AuPd surface was found to follow first-order kinetics. Interestingly, the catalytic activity of the HIF-AuNR@AuPd rod end was explicitly distinguished from that of the rod body, owing to the very different SERS activities at the two positions.

EXPERIMENTAL SECTION

Materials Synthesis. To synthesize HIF-AuNR@AuPd, AuNRs were first prepared using the well-established seed-mediated method.[11] Then, $HAuCl_4$ (0.01 M, 0.03 mL), Na_2PdCl_4 (0.01 M, 0.02 mL), and ascorbic acid (0.1 M, 0.2 mL) were sequentially added into a purified AuNR solution (2 mL, ∼0.4 nM). The obtained mixture was gently shaken for 10 s and then left under static conditions at room temperature for 3 h. The resulting hydrosol was washed by repeated centrifugation (5000 rpm, 10 min) and redispersed in H_2O three times. Several other nanostructures, including Au nanopolyhedron (AuNP), AuNP coated with a high-index {12 5 3} faceted Pd shell (HIF-AuNP@Pd), AuPd alloy nanooctahedron with {111} facets exposed (AuPd-Oct), Pd-coated Au nanocrystals with a nearly spherical morphology (Spherical Au@Pd), and Pd-coated AuNR with a shell thickness of ∼1 and ∼5 nm (denoted as AuNR@Pd-1 nm and AuNR@Pd-5 nm, respectively), were also synthesized. Their synthetic procedures are presented in the Supporting Information (SI).

Characterizations. Extinction spectra were taken on a Varian Cary 5000 UV−vis−NIR spectrophotometer. X-ray photoelectron spectroscopy (XPS) spectra were obtained using the Axis Ultra DLD system with Al Kα X-ray radiation (1486.6 eV). Scanning electron microscopy (SEM) was run on a high-resolution FEI Magellan 400L scanning electron microscope operated at 2 kV. Low-magnification transmission electron microscopy (TEM) images were acquired on a FEI-Tecnai T12 microscope operated at 120 kV. Ultramicrotomy was employed using a Leica EM UC6 ultramicrotome. Aberration-corrected high-angle-annular-dark-field (HAADF) scanning (S)TEM imaging, energy dispersive X-ray spectroscopy (EDX) mapping, and electron energy loss spectroscopy (EELS) mapping were carried out on a cubed FEI Titan G^2 electron microscope equipped with both a probe-corrector and a monochromator operated at 300 kV. The probe convergence angle was 24.9 mrad, and the inner detector angle was 76 mrad. A probe size of 0.8 Å and energy-resolution of 0.17 eV as measured from the full-width-at-half-maximum (fwhm) of the zero-loss peak (ZLP) were achieved. High-resolution TEM imaging and STEM tomography were carried out on a FEI-Titan ST electron microscope operated at 300 kV. An electron tomography tilt series from −75° to 75° at 1° intervals was first aligned and then reconstructed to a 3-D volume using the SIRT function in the FEI Inspect 3D software. The 3-D volume rendering, density segmentation and isosurface construction were then achieved by the Avizo software. The Raman spectra were recorded on a Horiba Jobin Yvon LabRAM HR-800 spectrophotometer coupled to an Olympus confocal microscope (BX41) with a ×50 objective (NA = 0.50) in the backscattering configuration with 532 and 785 nm laser excitations. Optical density filters and a constant acquisition time of 10 s were used for the measurements.

Colloidal SERS Measurements. AuNPs, HIF-AuNP@Pd, AuPd-Oct, AuNRs, AuNR@Pd-1 nm, AuNR@Pd-5 nm, and HIF-AuNR@AuPd were each incubated with an ethanol solution of 4-NTP (10^{-4} M) overnight to form colloidal suspensions with roughly identical particle concentrations. Enhancement factors (EFs) were calculated on the basis of the Raman spectrum of a pure 4-NTP solution (0.1 M) collected under the same experimental conditions (see SI for calculation details).

***In Situ* Monitoring of the Hydrogenation of 4-NTP with SERS.** The reactions were performed in a vertically oriented reaction chamber equipped with the Raman spectroscope under 785 nm laser excitation (laser power 2 mW at sample). The planar detection platforms mounted in the chamber were made by drop-casting a film of desired NCs on Si substrates (5 mm ×5 mm). The platforms were immersed into an ethanol solution of 4-NTP (10^{-2} M) for 12 h, followed by repeated rinsing with ethanol. These treatments yielded a monolayer of 4-NTP chemisorbed on the platform surface, as evidenced by the disappearance of the characteristic S−H stretching Raman band at 2550 cm^{-1}.[12] The reactions were performed at room temperature with 10 sccm of H_2/N_2 flow continuously introduced to the chamber. Successive SERS spectra were collected during the reaction until there were no noticeable changes between adjacent spectra.

RESULTS AND DISCUSSION

We chose single-crystalline AuNRs with a moderate aspect ratio (∼4) as seeds to prepare HIF-AuNR@AuPd because at this ratio, the longitudinal SPR are localized on the rod ends without antinodes formed in the body, which was important for our platform design, as discussed later. As shown in Figure 1a, the synthesized AuNRs had uniform sizes and aspect ratios (length = (78.6 ± 6.7) nm, width = (17.9 ± 1.6) nm, and aspect ratio = 4.3 ± 0.5) (see Figure S1 for the statistics). Traditional morphological models describe a single-crystalline

dx.doi.org/10.1021/ja4004602 | J. Am. Chem. Soc. 2013, 135, 8552−8561

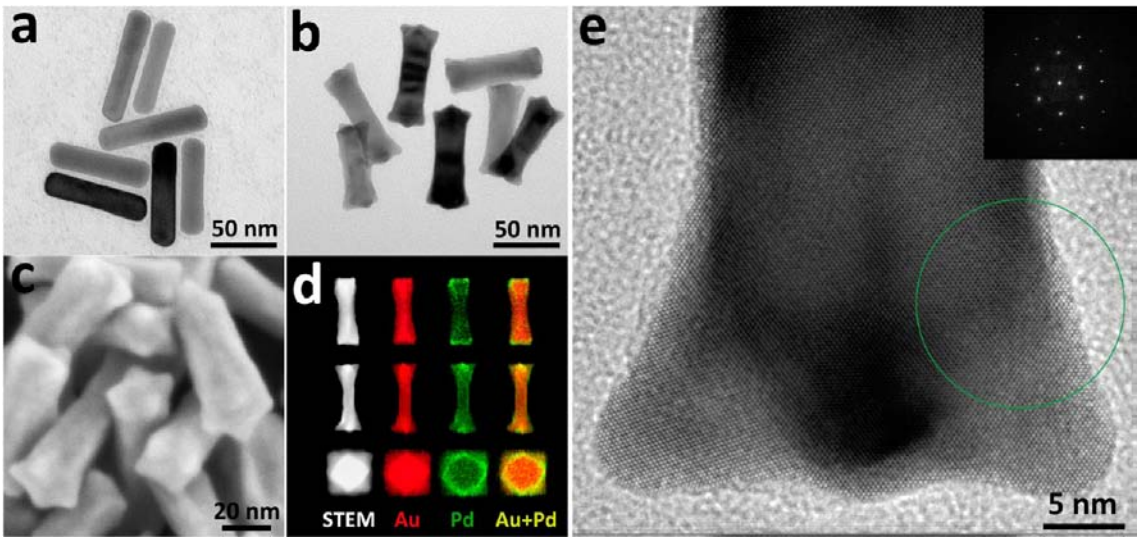

Figure 1. (a) TEM image of the AuNR seeds. (b) TEM image and (c) SEM image of the HIF-AuNR@AuPd nanorods. (d) HAADF-STEM images of HIF-AuNR@AuPd nanorods taken along the [100], [110], and [001] axes (the first column, from the top down), and the corresponding elemental mappings for Au (the second column) and Pd (the third column); the last column shows combined mappings, in which the simultaneous presence of Au and Pd appears yellowish. (e) HRTEM image of HIF-AuNR@AuPd taken at a rod end along the [110] axis. The inset is a fast Fourier transform diffractogram of the marked area, showing the perfect epitaxial growth of the horn from the rod body.

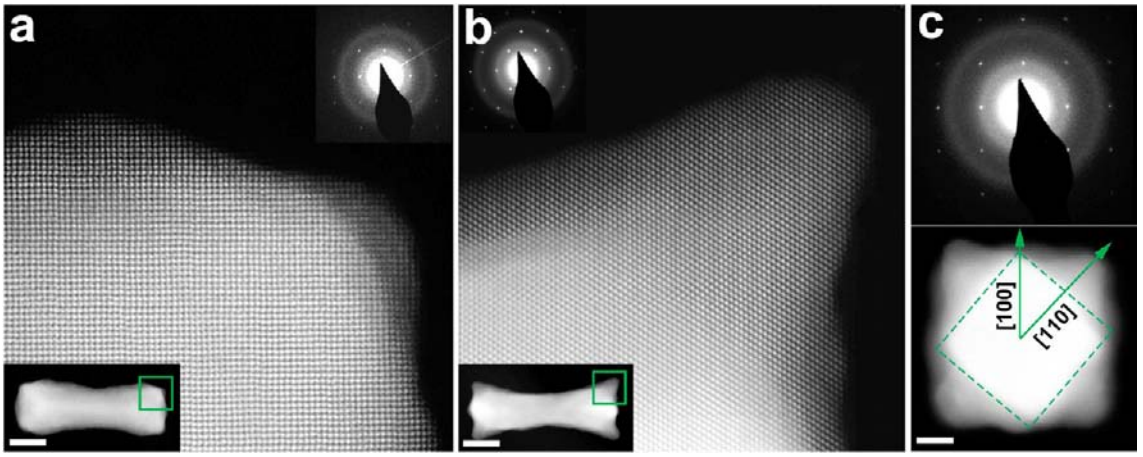

Figure 2. (a,b) SAED patterns (insets) and high-resolution HAADF-STEM images of a HIF-AuNR@AuPd nanorod taken along (a) the [100] and (b) the [110] axes. The corresponding low-magnification images are also provided as insets, in which the marked regions correspond to the high-resolution images. (c) SAED pattern (upper) and HAADF-STEM image (lower) of a HIF-AuNR@AuPd nanorod taken along the [001] axis (i.e., along the rod axis). The scale bars represent 20 nm in (a,b) and 5 nm in (c).

AuNR as an octagonal prism enclosed by four {100} and four {110} side facets.[13] However, two recent independent studies[14] demonstrated that contrary to this long-held model, AuNRs are actually enclosed by eight symmetry-equivalent high-index side facets of the {5 12 0} family. One of these studies further determined by using electron tomography that the rod ends terminated in a pyramid with {130} facets, and each pyramid was connected to the rod sides by four small {5 12 0} "bridging" facets (Figure S2).[14a] Here, we investigated the morphology of AuNR seeds by simply using ultramicrotomy for HRTEM sample preparation, which allowed direct imaging of the octagonal cross section of the AuNRs to identify their side facets (Figure S3). Our result accorded with the new model.

The design for HIF-AuNR@AuPd originated from the attempt to prepare a plasmonic and catalytic bimetallic nanostructure by depositing Pd onto AuNR seeds. We found that, provided with sufficient Pd precursors, a continuous Pd shell can be formed on individual AuNRs (Figure S4a), whereas a small amount of precursor only gives rise to discrete Pd particles that are selectively anchored on the two ends of AuNRs, specifically at the rod corners where two side facets and one bridging facet meet (Figure S4b). HRTEM showed that these Pd particles had the same crystalline orientations as AuNR had, suggesting an epitaxial growth mode (Figure S4c–e). The observed preferential deposition of Pd on AuNR ends is thermodynamically sensible, as low-coordinated sites (e.g., crystal corners) are favorable for heterogeneous nucleation. Inspired by this result, we supposed that it would be possible to grow Au–Pd alloy site-specifically on the ends of AuNR through the codeposition of Au and Pd.

As revealed in the TEM image, the as-prepared HIF-AuNR@AuPd NCs remained rod-shaped without significant changes in the aspect ratio (despite being slightly fatter) relative to the AuNR seeds, but they featured newly grown "horns" on the rod

dx.doi.org/10.1021/ja4004602 | J. Am. Chem. Soc. 2013, 135, 8552–8561

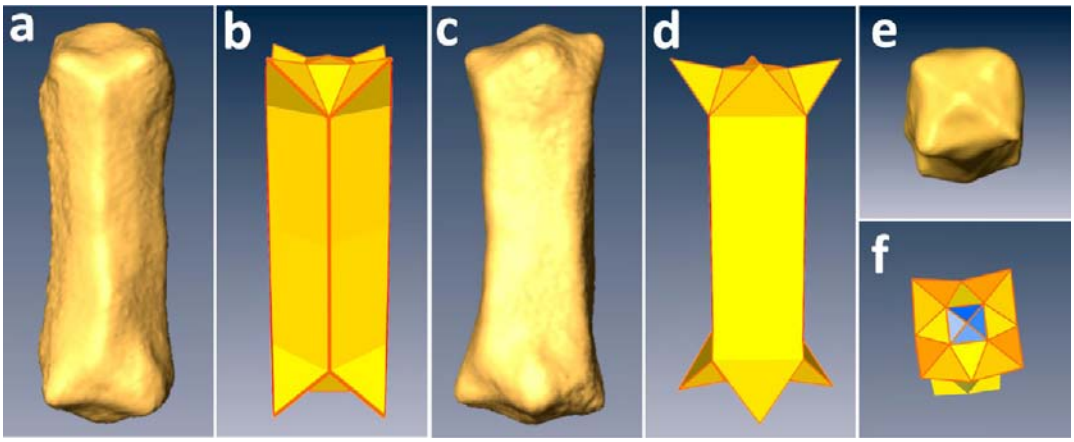

Figure 3. Surface-rendered visualization of the HIF-AuNR@AuPd nanorod morphology reconstructed by HAADF-STEM tomography, viewed along (a) the [100], (c) the [110], and (e) the [001] axes. The corresponding schematic morphology models are given for reference (b, d, and f). Note that the viewing angle of (e) and (f) deviates slightly from the exact [001] axis to show the surface features more clearly, and a top-end pyramid is labeled with blue color in (f).

ends (Figures 1b andS5). The SEM image further indicated that there were four horns at each end of each nanorod (Figure 1c). Selected-area electron diffraction (SAED) demonstrated that each individual HIF-AuNR@AuPd nanorod was a single crystal with its rod axis parallel to the [001] zone axis, and the HRTEM image accordingly showed perfect epitaxial growth of the horns from the AuNR (Figure 1e). HAADF-STEM images of the [100] and [110] projections (Figure 2a,b), which were taken from a same nanorod by tilting the specimen along its rod axis by 45°, confirmed the single-crystal nature of HIF-AuNR@AuPd. They also showed that the "horn" feature was more remarkable in the [110] projection. To clarify the 3-D structure of HIF-AuNR@AuPd, it is crucial to acquire images along the rod axis, i.e. along the [001] direction, which requires a specimen with "standing" nanorods. To achieve this, we employed ultramicrotomy for specimen preparation. Figure 2c shows a HAADF-STEM image of a HIF-AuNR@AuPd nanorod taken along the rod axis, in which four horns at the corners can be easily distinguished from the rod body in the center region by the image contrast arising from different specimen thicknesses. The center region with brighter contrast appears as a square with the edges normal to the four ⟨110⟩ directions, as determined by SAED (Figure 2c), suggesting that the rod body of HIF-AuNR@AuPd is bound by four {110} lateral low-index facets (LIFs). Furthermore, by analyzing the HRTEM images of different orientations, we identified that the horns grow along the ⟨111⟩ directions (see Figure S6 for details).

The information gained from the SAEDs and 2-D HREM images of different orientations is essentially sufficient for delineating a basic 3-D structural model of a HIF-AuNR@AuPd nanorod. Advancing a step, we employed HAADF-STEM tomography to discern more details, such as the top-end fine structures of the nanorod and the side facets of the horns. In comparison with classic bright-field TEM tomography, HAADF-STEM tomography gives much reduced diffraction contrast (unwanted in tomography) along with the enhanced *Z*-contrast and is therefore particularly advantageous for reconstructing crystalline metallic nanostructures. Specifically, a series of STEM images was continuously acquired by tilting the specimen over a range of −75° to +75° with regular intervals of 1°. The obtained image series was aligned and processed to reconstruct a "volume" that was visualized through surface rendering or as a set of slices to show the local structures (Figures 3 and 4a and Movies 1 and 2). The reconstructed 3-D tomographic images matched the 2-D (S)TEM images of the same projections well (Figures 2 and 3) and clearly verified that a HIF-AuNR@AuPd nanorod has four {110} side facets enclosing the rod body and four horns at each rod end protruding along the ⟨111⟩ directions. More importantly, tomography helps to identify local structural features that cannot be easily recognized from 2-D images. For example, the reconstructed 3-D image showed that along the [00±1] directions (Figure 3e), the rod end terminated in a flattened pyramid with four equivalent side faces that were parallel to the [100] and [010] directions. Hence, these faces became "edge-on" when the nanorod was projected along a [100] zone axis and their Miller indices were readily determined from the HR-STEM image. Figure 4b clearly shows that the side surface of a top-end pyramid was terminated by a {0 5 12} facet, which can be visualized as a combination of two {001} terraces of three atomic widths, three {001} terraces of two atomic widths, and four monatomic {010} step risers. Moreover, the reconstructed image shows that the "horns" are nearly tetrahedral with three exposed side faces extending smoothly from the horn vertex to the body and top-ends of the nanorod. Slicing at different positions along a "horn" (the slices are perpendicular to the [111] axis) generates a set of trigonal cross sections with each angle close to 60°, suggesting that the three side faces of each "horn" are topologically equivalent (Figure 4a). Because the [111] axis of a cubic structure coincides with its threefold symmetry axis, the three side faces are also crystallographically equivalent. Since one of these three side faces is edge-on when the nanorod is projected along a [110] zone axis, its index can be determined by measuring the angle between its normal and a known direction, e.g. the [1−10] direction. The statistical results of horns from 50 rods show that this angle ranges from 10° to 17°, corresponding to the indices of {11*l*} ($0.25 < l < 0.43$). As an example, Figure 4c shows a HR-STEM image of a "horn" taken along the [110] axis, in which the edge-on side face is indexed as {441}. These results demonstrate the presence of adequate high-index facets at the rod ends of HIF-AuNR@AuPd. The complete model of HIF-AuNR@AuPd is presented and compared with that of AuNR in Figure S2.

dx.doi.org/10.1021/ja4004602 | *J. Am. Chem. Soc.* 2013, 135, 8552−8561

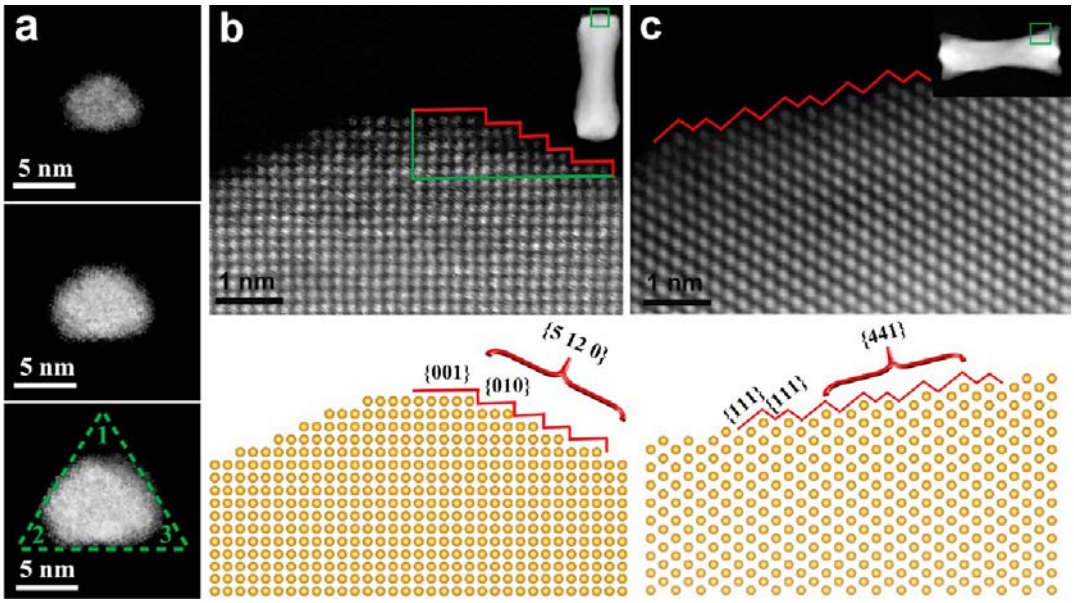

Figure 4. (a) Three slices of the "horn" along the [111] axis with an interval of 1 nm extracted from the HAADF-STEM tomography-reconstructed volume. (b) HR-STEM image of a HIF-AuNR@AuPd nanorod taken along the [100] axis and the schematic atom arrangement, showing that the top-end pyramid has {0 5 12} side facets. (c) HR-STEM image of a HIF-AuNR@AuPd nanorod taken along the [110] axis and the schematic atom arrangement, showing that the horn has a {441} side facet. Low-magnification images are presented in the insets to show the regions (marked) from where the high-resolution images were taken.

We combined EDX elemental analysis with STEM to investigate the distribution of Pd and Au within HIF-AuNR@AuPd. The EDX mappings of different orientations all demonstrate that the horns are comprised of uniformly distributed Pd and Au (Figure 1d). These results along with the uniform contrast of the high-resolution HAADF-STEM images (Figure 2a,b) indicate the alloy nature of the horns. The EDX mappings also show that the four {110} lateral faces of the nanorod are terminated with thin layers of Au−Pd alloy (Figure 1d). The Pd/Au atomic ratio on the surface of HIF-AuNR@AuPd is 53:47, as determined by XPS.

To investigate the influence of the growth of Au−Pd horns on the SPR of AuNR, we first compared the UV−vis spectra of different materials (Figure 5a). The original AuNRs exhibited two extinction bands centered at 513 and 837 nm, corresponding to a weak transverse surface plasmon (TSP) resonance and a strong longitudinal surface plasmon (LSP) resonance, respectively. We found that, in accordance with literature,[15] coating AuNRs with a thin shell (~1 nm) of Pd dramatically weakened and broadened the extinction bands and that this effect became more severe with an increase in the Pd shell thickness. In contrast, modest damping and a slight red-shift of SPR was observed for HIF-AuNR@AuPd. This can be explained by the fact that the dielectric function of Au−Pd alloy is a linear combination of the dielectric functions of Au and Pd, and it therefore has a smaller imaginary part throughout the visible and near-infrared regime to render a weaker damping effect, as compared with the case of pure Pd.

UV−vis spectroscopy uses a plane-wave incidence that only excites the dipole-allowed SP modes ("bright" modes).[16] However, the dipole-forbidden multipolar SP modes ("dark" modes) may also contribute to the activity of a planar SERS platform, owing to the symmetry-breaking of the charge density distributions by interparticle or substrate-mediated SP coupling.[17] To investigate various SP-associated near-fields and their distributions, which requires both high spatial and energy resolution, we employed a C_s-corrected and monochromated electron beam (a sub-angstrom probe with an 0.17 eV energy spread) to excite all the SP modes in the nanostructures.[18] The spatially resolved EELS spectra clearly show that in AuNR with an aspect ratio of ~4, there is an intense LSP excitation at 1.8 eV concentrated near the rod ends and several overlapped weak SP excitations at ~2.5 eV, which are uniformly distributed near the rod body and possibly associated with different transverse modes (Figure 5b). In HIF-AuNR@AuPd, the two types of SP modes both experience a red-shift of 0.3−0.4 eV, while the LSP mode remains dominant (Figure 5b). We directly visualized the distributions of the two types of different SP modes in AuNR and HIF-AuNR@AuPd by EELS mapping with an energy filter at their respective excitation positions with a 0.2 eV window. As shown in Figure 5c−e, typical dipolar SPR patterns, which show highly localized strong fields at the two rod ends, were observed in the "bright" LSP mode in both AuNR and HIF-AuNR@AuPd. In the latter case, EELS mappings were performed along two major zone axes (i.e., [100] and [110]) and the results were consistent (Figure 5d,e). Also, the weak fields of those TSP modes exhibited similar uniform distributions in both kinds of nanorods (Figure 5c−e). These results confirmed that the growth of Au−Pd alloy horns did not cause marked variations in the intensity or spatial distribution of various SP modes of the AuNRs. Since no "dark" SP modes with considerable field intensities were observed, the SERS activity was mostly contributed by the dipolar LSP mode. We thus concluded that a sensitive SERS detection can be achieved in HIF-AuNR@AuPd by exciting the LSP mode to render strong field enhancement at the two rod ends.

The present discussion demonstrated that for an individual HIF-AuNR@AuPd nanorod, much stronger SP fields exist at the rod ends than at the rod body. However, the nanorods agglomerate when used as a planar SERS platform. In that case, whether or not the site-dependent SERS effect still holds when

dx.doi.org/10.1021/ja4004602 | J. Am. Chem. Soc. 2013, 135, 8552−8561

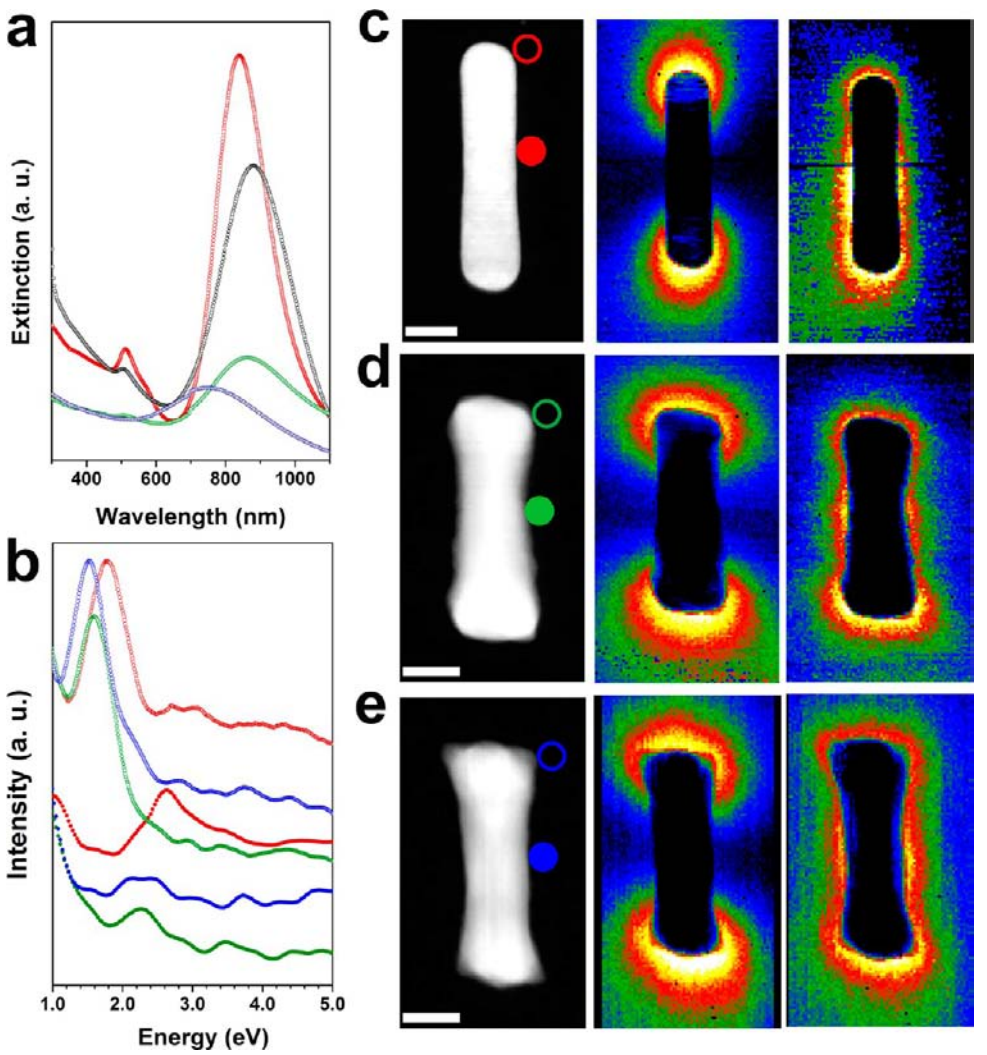

Figure 5. (a) UV−vis extinction spectra of AuNR (red), HIF-AuNR@AuPd (black), AuNR@Pd-1 nm (green), and AuNR@Pd-5 nm (blue). (b) EELS spectra of AuNR and HIF-AuNR@AuPd sampled from different positions (refer to (c−e), where filled and empty circles in different colors labeled in the STEM images indicate the origin of each EELS spectrum with the same symbol). (c−e) STEM images (left), LSP mappings (middle), and TSP mappings (right) of (c) AuNR and (d,e) HIF-AuNR@AuPd with different orientations: (d) [100] and (e) [110]. The energy window for mapping is 0.2 eV and the filtered energy positions of LSP/TSP modes for AuNR and HIF-AuNR@AuPd are 1.8/2.5 and 1.5/2.2 eV, respectively. Scale bars in (c−e) signify 20 nm.

"hot spots", which could lead to further SERS enhancement, are formed at particle junctions should be considered.[19] It was reported that under the circumstance of particle agglomeration, the SERS enhancement mainly resulted from the dipolar component of the hybridized plasmonic field.[17a] A study of dipolar plasmonic coupling between AuNRs with different geometries (e.g., end-to-end, side-by-side, L-type, or T-type) further indicated that the couplings between LSP modes were predominant over LSP-TSP or TSP-TSP coupling[20] and the most intensive field enhancement was still localized on the rod ends that decayed rapidly with distance from the crystal surface. We therefore deduced that when HIF-AuNR@AuPd is used as a planar platform, the signal enhancement is primarily a contribution by the rod ends.

The unique morphological and compositional design of HIF-AuNR@AuPd makes it useful for *in situ* monitoring a catalytic reaction via SERS. In a proof-of-concept experiment, we investigated the Pd-catalyzed hydrogenation of 4-nitrothiophenol (4-NTP) to 4-aminothilphenol (4-ATP) at room temperature (inset of Figure 6a). Specifically, 4-NTP molecules first formed a monomolecular layer on the surface of HIF-AuNR@AuPd through chemisorption,[12] where they were on-site reduced to 4-ATP molecules by Pd upon the subsequent introduction of a hydrogen flow. We note that Au has shown to be catalytically inert for this reaction. The SERS spectrum of the 4-NTP monolayer exhibited characteristic bands at 854, 1076, 1334, and 1571 cm^{-1} that were respectively assigned to C−H wagging, C−S stretching, O−N−O stretching, and the phenyl-ring mode (Figure 6a).[12a] The intensities of the R-NO_2-associated bands decreased with the conversion of 4-NTP to 4-ATP, and concomitantly two characteristic bands of 4-ATP at 1486 and 1587 cm^{-1} emerged (Figure 6a).[21] Since hydrogen dissociative activation on Pd is a very fast process even at room temperature,[22] the subsequent reduction of 4-NTP by the activated hydrogen species should be a kinetically relevant step. Hence, the reaction kinetics can be quantified from the intensity evolution of the SERS bands of 4-NTP, which corresponds to its concentration variation.

We first evaluated the SERS activities of different nanostructures in colloidal solution (Figure S7; see Exper-

dx.doi.org/10.1021/ja4004602 | J. Am. Chem. Soc. 2013, 135, 8552−8561

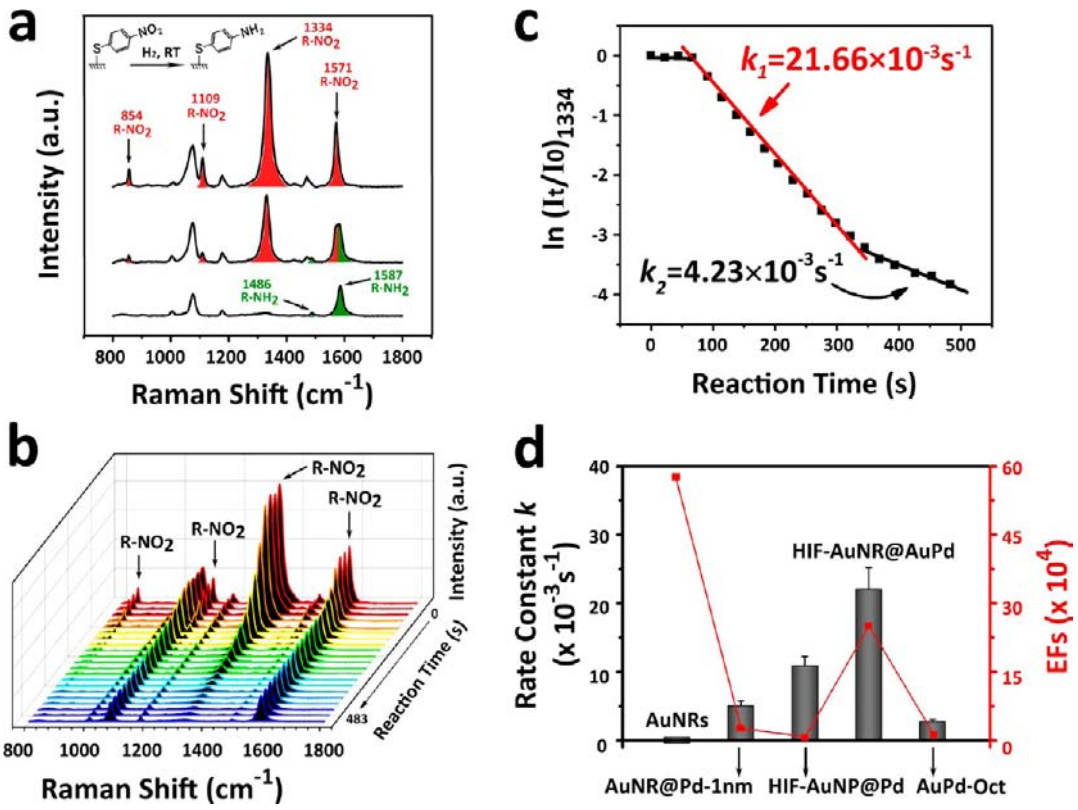

Figure 6. (a) SERS spectra of the hydrogenation of chemisorbed 4-NTP to 4-ATP over a Pd catalyst at the initial stage with reactant 4-NTP (upper), the final stage with product 4-ATP (bottom) and an intermediate stage with the coexistence of the two compounds (middle). (b) Successive SERS spectra of the reduction of 4-NTP by H_2 collected on a planar platform made of HIF-AuNR@AuPd NCs. (c) A plot of the logarithm of the Raman intensity at 1334 cm^{-1} versus reaction time ($\ln(I_t/I_0) \sim t$ plot) for the catalytic hydrogenation of 4-NTP on HIF-AuNR@AuPd. (d) Normalized rate constants and SERS EF values of AuNR, AuNR@Pd-1 nm, HIF-AuNP@Pd, HIF-AuNR@AuPd, and AuPd-Oct.

imental Section for the descriptions of various nanostructures and SERS measurement details). The excitation wavelength for each material was chosen based on its extinction spectra. The results show that AuNR exhibits ~40-fold higher SERS activity than AuNP exhibits (enhancement factor (EF): 5.7×10^5 vs. 1.5×10^4). In accordance with the conclusion drawn earlier from the extinction spectra (Figure 5a) that coating Au NCs with Pd severely suppresses the SERS activity, the calculated EF values for HIF-AuNP@Pd, AuNR@Pd-1 nm, and AuNR@Pd-5 nm were 3.6×10^3, 2.4×10^4, and 4.5×10^3, respectively. The EF of AuPd-Oct was determined to be 5.8×10^3. Among all the tested bimetallic nanostructures, HIF-AuNR@AuPd had the highest EF of 2.5×10^5 (Figure 6d). These results demonstrate that for the preparation of a bifunctional nanostructure, incorporating AuPd alloy instead of pure Pd as a catalytic component can effectively mitigate the plasmonic damping in Au. As addressed earlier, when used in a solid form for reaction monitoring, HIF-AuNR@AuPd would provide additional sensitivity due to the "hot spot" effect. We attempted to evaluate this effect and the results showed that the "hot spot" involving SERS activity was approximately 1 order of magnitude higher than that of a colloidal solution, giving an EF of 1.6×10^6.

Owing to its high SERS activity, the evolution of 4-NTP to 4-ATP over HIF-AuNR@AuPd was explicitly reflected in a series of *in situ* Raman spectra collected during the reaction (Figure 6b). Since the chemisorbed 4-NTP molecules formed a monolayer on the surface of the catalysts, the integrated intensity of the strongest band at 1334 cm^{-1} (denoted as I_t) was proportional to the surface coverage percentage, θ, of 4-NTP (i.e., $\theta_{[4\text{-NTP}]}(t) = I_t/I_0$, where I_0 refers to the initial intensity at full coverage). Approximating the average coordination number of Pd/Au-4-NTP to be 1 for simplicity, the equation of turnover frequency (TOF) normalized to the fraction of Pd active sites at the catalyst surface, which was derived from the XPS Au/Pd atomic ratio, can be expressed as

$$\text{TOF}\ (s^{-1}) = -\frac{\partial\theta_{[4\text{-NTP}]}(t)}{\partial t}\frac{1}{\eta} = k[H_2]^m\theta_{[4\text{-NTP}]}(t)^n \quad (1)$$

where m, n, and η are the reaction order of $[H_2]$ and [4-NTP] and the fraction of Pd, respectively. Since hydrogen activation is facilitated on Pd and the diffusion limitation is negligible owing to a large linear velocity of hydrogen flow, we expected the reaction order of $[H_2]$ to be zero, which was confirmed by the constant reaction rates under different hydrogen partial pressures (>0.5 bar). Considering $m = 0$, the rate eq 1 can be simplified as follows:

$$\text{TOF}\ (s^{-1}) = -\frac{\partial\theta_{[4\text{-NTP}]}(t)}{\partial t}\frac{1}{\eta} = k\theta_{[4\text{-NTP}]}(t)^n \quad (2)$$

$$\Rightarrow \ln\left(-\frac{\partial(I_t/I_0)}{\partial t}\frac{1}{\eta}\right) = n\ln(I_t/I_0) + \ln k \quad (3)$$

Hence, both the reaction order of 4-NTP and the rate constant, k, can be calculated on the basis of the (I_t/I_0) evolution diagram. A typical diagram (Figure 6b) shows an initial delay of ~60 s before the reduction becomes evident. Such an induction

dx.doi.org/10.1021/ja4004602 | J. Am. Chem. Soc. 2013, 135, 8552−8561

period could result from the filling-up of hydrogen in the reaction chamber and/or catalyst activation by reducing the pre-oxidized surface of Pd.[23] A linear regression analysis of the $\ln(-(\partial(I_t/I_0))/(\partial t)(1/\eta))$ versus $\ln(I_t/I_0)$ plot gives $n = 1.07 \pm 0.02$, suggesting first-order kinetics (Figure S8). Hence, eq 3 becomes

$$\ln(I_t/I_0) = -k\eta t \quad (4)$$

A reaction rate constant of $k = 21.66 \times 10^{-3}$ s^{-1} can thus be readily derived from the linearly fitted slope of the $\ln(I_t/I_0) \sim t$ plot (Figure 6c). It is noteworthy that the validity of our method is based on two prerequisites: (i) the SERS spectra series are collected from exactly the same position, which was satisfied by carefully operating a confocal Raman spectroscope; and (ii) 4-NTP molecules form a uniform monolayer on the metallic nanocrystal surface, which is well characterized and generally accepted.[12] It was reported that 4-NTP or 4-ATP could undergo SPR-induced photocatalytic dimerization to form dimercaptoazobenzene (DMAB) on silver and gold surfaces under specific conditions.[21,24] In our experiments, however, we did not observe the formation of DMAB during the reaction as indicated by the SERS spectra (Figure 6a). This was possibly due to the different excitation conditions that we used (785 nm laser, 2 mW power). Moreover, we found that without introducing hydrogen, the SERS spectrum of 4-NTP did not change over time. We therefore concluded that no DMAB molecules were involved in the hydrogenation reaction of 4-NTP and our above-discussed kinetic study was valid.

Using the same method, we also determined the rate constants of some other metallic nanostructures for the hydrogenation of 4-NTP (Figures 6d and S9). The results show that AuNR was not able to catalyze this reaction. This is consistent with previous studies,[1b,24c,25] which showed that Au NCs with sizes larger than 10 nm were catalytically inert for this reaction even using stronger reducing agent sodium borohydride. AuNR@Pd-1 nm was active because of the Pd shell, giving a k value of $(5.07 \pm 0.69) \times 10^{-3}$ s^{-1}; with a similar core−shell structure, HIF-AuNP@Pd was more active [$k = (10.88 \pm 1.37) \times 10^{-3}$ s^{-1}] than AuNR@Pd-1 nm, likely due to its high-index surfaces. Overall, HIF-ANR@AuPd exhibited the highest catalytic activity among all the tested materials. In addition to the high-index facets, the Au−Pd alloy nature of the surface of HIF-ANR@AuPd is another reason for its superior activity, because the 4d state of Pd is remarkably populated through Pd4d−Au5d hybridization upon alloying,[26] and this favors the electrophilic hydrogenation of 4-NTP. AuPd-Oct with alloyed (Au/Pd ≈ 1:1 in molar) but low-index {111} surfaces was much less active [$k = (2.74 \pm 0.32) \times 10^{-3}$ s^{-1}] than HIF-ANR@AuPd, further illustrating the crystal-facet-dependent catalytic activities.

It is very interesting to note that in the $\ln(I_t/I_0) \sim t$ plot of HIF-AuNR@AuPd (Figure 6c), there is an inflection point at $t \approx 360$ s, after which the reaction apparently becomes slower ($k = 4.23 \times 10^{-3}$ s^{-1}). This phenomenon implies the coexistence of two kinds of catalytic sites with different activities in HIF-AuNR@AuPd. According to its 3-D structure described earlier, the high-index faceted horns at the rod ends are supposed to have higher catalytic activity than the rod body that exposes low-index {110} facets. More interestingly, the Raman signals of the molecules residing on the rod ends are significantly amplified by the LSP resonance, while the signals of the molecules adsorbed by the rod body are only slightly enhanced by the TSP under off-resonance conditions. The fast conversion of 4-NTP taking place at the rod ends was first captured by the rapidly changed SERS spectra, to which the signals from the rod body made negligible contributions due to the much weaker enhancement effect of the TSP. When the 4-NTP molecules at the rod ends were consumed, the slower conversion of 4-NTP at the rod body became visible. Thus, the catalytic activities at different positions of HIF-AuNR@AuPd were clearly distinguished and accurately determined by utilizing the anisotropic distribution of SPRs to achieve site-dependent field enhancements. It should be noted that the precondition for discriminating two kinds of catalytic sites on HIF-AuNR@AuPd is that the rod ends and the rod body have remarkable differences in both catalytic activity and plasmonic activity. As a negative control, we prepared another nanostructure that consists of Pd-coated Au nanocrystals with nearly spherical morphologies (spherical Au@Pd)[27] and investigated its reaction kinetics using the *in situ* SERS method described above. Because this structure has a nearly isotropic SP field distribution and no remarkably distinct catalytically active sites, only one reaction rate constant, k, was observed (Figure S9). Actually, the nanostructures that we discussed earlier, i.e. AuNR@Pd-1 nm and HIF-AuNP@Pd, can also be regarded as "controls" in this sense. In these structures, the exposed facets are approximately equivalent or one type of crystal facets are predominant in term of surface area. Accordingly, only one rate constant can be explicitly determined for each of them despite their anisotropic SP field distributions (Figure S9). Moreover, we repeated the kinetic study using another two HIF-AuNR@AuPd platforms, and found that the reaction rate constants of the HIFed sites determined from three independent experiments accord closely with each other (21.66×10^{-3}, 18.11×10^{-3}, and 19.12×10^{-3} s^{-1}, respectively), despite the different initial absolute SERS intensities (Figure S10). These results clearly demonstrate that the kinetic parameters determined with this method are intrinsic and unaffected by the laser probe position or hot spot effect, and provide strong evidence for the reliability of our conclusions on the reaction kinetics.

Finally, we would clarify three additional points regarding the catalyst assessment method that we used in this study: (i) For the first-order kinetics, the reaction rate constant k can actually be determined from the absolute SERS intensities (I_t) as the slope of the $\ln(I_t) \sim t$ linear relationship. However, we prefer to use relative intensities (I_t/I_0), which are associated with the surface coverage percentages of the reactant and thus in principle allow the determination of TOF in addition to the rate constant. (ii) For the HIF-AuNR@AuPd that contains two kinds of catalytic active sites with different SERS activities, the two k values can both be directly deduced from the slopes of the two linear segments in the $\ln(I_t/I_0) \sim t$ plot. To determine the TOF of the rod body, however, one should redefine the surface coverage using a different initial SERS intensity (I_0'), which can be derived by extrapolating the second linear segment to get the y-intercept. (iii) Due to the much stronger enhancement at the rod ends, the SERS intensities used for calculating the rate constant of the rod body (i.e., the second k) inevitably involve the contribution from the residual 4-NTP molecules at the rod ends despite their very low concentration. This leads to a lower accuracy in k determination for the rod body than for the rod ends.

dx.doi.org/10.1021/ja4004602 | J. Am. Chem. Soc. 2013, 135, 8552−8561

CONCLUSIONS

The integration of catalytic activity with the surface plasmonic property enables HIF-AuNR@AuPd to serve as a bifunctional platform to monitor catalytic reactions *in situ* with SERS. The rod-like morphology of HIF-AuNR@AuPd leads to strong LSP resonance localized at the rod ends, where there are high-index-faceted horns providing highly active catalytic sites. The Au−Pd alloy nature of the horns not only enhances the catalytic activity but also circumvents plasmonic damping to a great extent. Using HIF-AuNR@AuPd to catalyze and at the same time to monitor the hydrogenation of 4-NTP, we directly determined the kinetics of this reduction and distinguished two kinds of catalytic active sites with different activities. These results suggest exciting prospects for studying catalytic reaction processes on catalyst surfaces with high sensitivity. As we were finalizing this manuscript, we noticed a new publication by Kneipp et al. that reported a SERS-assisted reaction kinetics study using a physical mixture of separate gold and platinum nanoparticles.[25] In this work, we developed a well-defined composite nanostructure that combines the plasmonic and catalytic activities in one entity in the form of a single crystal rather than separate particles, which can avoid the local inhomogeneous distribution of two kinds of particles and facilitate in-depth structure−property relationship studies.

ASSOCIATED CONTENT

Supporting Information

Experimental details and supporting figures (Figures S1−S10). This material is available free of charge via the Internet at http://pubs.acs.org.

Web-Enhanced Features

Movies 1 and 2, in .mpg format, are available online in the HTML version.

AUTHOR INFORMATION

Corresponding Author

yu.han@kaust.edu.sa

Author Contributions

§J.H. and Y.Z. contributed equally to this paper.

Notes

The authors declare no competing financial interest.

ACKNOWLEDGMENTS

This research was supported by baseline research funds to Y.H. from King Abdullah University of Science and Technology.

REFERENCES

(1) (a) Heck, K. N.; Janesko, B. G.; Scuseria, G. E.; Halas, N. J.; Wong, M. S. *J. Am. Chem. Soc.* **2008**, *130*, 16592. (b) Xie, W.; Herrmann, C.; Kompe, K.; Haase, M.; Schlucker, S. *J. Am. Chem. Soc.* **2011**, *133*, 19302. (c) Seo, D.; Park, G.; Song, H. *J. Am. Chem. Soc.* **2012**, *134*, 1221. (d) Larsson, E. M.; Langhammer, C.; Zoric, I.; Kasemo, B. *Science* **2009**, *326*, 1091. (e) Zou, S.; Williams, C. T.; Chen, E. K. Y.; Weaver, M. J. *J. Am. Chem. Soc.* **1998**, *120*, 3811. (f) Kim, H.; Kosuda, K. M.; Van Duyne, R. P.; Stair, P. C. *Chem. Soc. Rev.* **2010**, *39*, 4820.

(2) (a) Nie, S. M.; Emory, S. R. *Science* **1997**, *275*, 1102. (b) Pieczonka, N. P.; Aroca, R. F. *Chem. Soc. Rev.* **2008**, *37*, 946. (c) Kneipp, J.; Kneipp, H.; Kneipp, K. *Chem. Soc. Rev.* **2008**, *37*, 1052. (d) Fang, Y.; Seong, N. H.; Dlott, D. D. *Science* **2008**, *321*, 388.

(3) (a) Mazumder, V.; Chi, M.; More, K. L.; Sun, S. *Angew. Chem., Int. Ed.* **2010**, *49*, 9368. (b) Wang, L.; Yamauchi, Y. *J. Am. Chem. Soc.* **2010**, *132*, 13636.

(4) (a) Tian, N.; Zhou, Z.-Y.; Sun, S. G.; Ding, Y.; Wang, Z. L. *Science* **2007**, *316*, 732. (b) Lim, B.; Jiang, M. j.; Camargo, P. H. C.; Cho, E. C.; Tao, J.; Lu, X. M.; Zhu, Y. M.; Xia, Y. N. *Science* **2009**, *324*, 1302. (c) Jin, M. S.; Zhang, H.; Xie, Z. X.; Xia, Y. N. *Angew. Chem., Int. Ed.* **2011**, *50*, 7850. (d) Quan, Z.; Wang, Y.; Fang, J. *Acc. Chem. Res.* **2013**, *46*, 191. (e) Li, C.; Sato, R.; Kanehara, M.; Zeng, H.; Bando, Y.; Teranishi, T. *Angew. Chem., Int. Ed.* **2009**, *48*, 6883. (f) Yang, C. W.; Chanda, K.; Lin, P. H.; Wang, Y. N.; Liao, C. W.; Huang, M. H. *J. Am. Chem. Soc.* **2011**, *133*, 19993. (g) Kim, D.; Lee, Y. W.; Lee, S. B.; Han, S. W. *Angew. Chem., Int. Ed.* **2012**, *51*, 159. (h) Zhang, J.; Langille, M. R.; Personick, M. L.; Zhang, K.; Li, S. Y.; Mirkin, C. A. *J. Am. Chem. Soc.* **2010**, *132*, 14012. (i) Yu, Y.; Zhang, Q.; Liu, B.; Lee, J. Y. *J. Am. Chem. Soc.* **2010**, *132*, 18258. (j) Wang, F.; Li, C.; Sun, L. D.; Wu, H.; Ming, T.; Wang, J. F.; Yu, J. C.; Yan, C. H. *J. Am. Chem. Soc.* **2011**, *133*, 1106.

(5) (a) Stamenkovic, V. R.; Fowler, B.; Mun, B. S.; Wang, G.; Ross, P. N.; Lucas, C. A.; Markovic, N. M. *Science* **2007**, *315*, 493. (b) Ferrando, R.; Jellinek, J.; Johnston, R. L. *Chem. Rev.* **2008**, *108*, 845. (c) Norskov, J. K.; Bligaard, T.; Rossmeisl, J.; Christensen, C. H. *Nat. Chem.* **2009**, *1*, 37. (d) Liu, X. W.; Liu, X. G. *Angew. Chem., Int. Ed.* **2012**, *51*, 3311.

(6) (a) Xia, X.; Zeng, J.; McDearmon, B.; Zheng, Y.; Li, Q.; Xia, Y. *Angew. Chem., Int. Ed.* **2011**, *50*, 12542. (b) Hong, J. W.; Lee, S. U.; Lee, Y. W.; Han, S. W. *J. Am. Chem. Soc.* **2012**, *134*, 4565. (c) Lee, Y. W.; Kim, M.; Kang, S. W.; Han, S. W. *Angew. Chem., Int. Ed.* **2011**, *50*, 3466. (d) Kneipp, K.; Kneipp, H.; Kneipp, J. *Acc. Chem. Res.* **2006**, *39*, 443. (e) Huang, J. F.; Vongehr, S.; Tang, S. C.; Lu, H. M.; Shen, J. C.; Meng, X. K. *Langmuir* **2009**, *25*, 11890.

(7) (a) Nicoletti, O.; Wubs, M.; Mortensen, N. A.; Sigle, W.; van Aken, P. A.; Midgley, P. A. *Opt. Exp.* **2011**, *19*, 15371. (b) N'Gom, M.; Li, S. A.; Schatz, G.; Erni, R.; Agarwal, A.; Kotov, N.; Norris, T. B. *Phys. Rev. B* **2009**, *80*, 113411−1.

(8) (a) Chen, M.; Kumar, D.; Yi, C. W.; Goodman, D. W. *Science* **2005**, *310*, 291. (b) Enache, D. I.; Edwards, J. K.; Landon, P.; Solsona-Espriu, B.; Carley, A. F.; Herzing, A. A.; Watanabe, M.; Kiely, C. J.; Knight, D. W.; Hutchings, G. J. *Science* **2006**, *311*, 362. (c) Kesavan, L.; Tiruvalam, R.; Rahim, M. H. A.; bin Saiman, M. I.; Enache, D. I.; Jenkins, R. L.; Dimitratos, N.; Lopez-Sanchez, J. A.; Taylor, S. H.; Knight, D. W.; Kiely, C. J.; Hutchings, G. J. *Science* **2011**, *331*, 195. (d) Edwards, J. K.; Solsona, B.; N, E. N.; Carley, A. F.; Herzing, A. A.; Kiely, C. J.; Hutchings, G. J. *Science* **2009**, *323*, 1037.

(9) (a) DeSantis, C. J.; Peverly, A. A.; Peters, D. G.; Skrabalak, S. E. *Nano Lett.* **2011**, *11*, 2164. (b) DeSantis, C. J.; Sue, A. C.; Bower, M. M.; Skrabalak, S. E. *ACS Nano* **2012**, *6*, 2617.

(10) Kan, C.; Cai, W.; Li, C.; Zhang, L.; Hofmeister, H. *J. Phys. D: Appl. Phys.* **2003**, *36*, 1609.

(11) (a) Jana, N. R.; Gearheart, L.; Murphy, C. J. *J. Phys. Chem. B* **2001**, *105*, 4065. (b) Nikoobakht, B.; El-Sayed, M. A. *Chem. Mater.* **2003**, *15*, 1957. (c) Sun, Z. H.; Bao, Z. H.; Fang, C. H.; Wang, J. F. *Langmuir* **2012**, *28*, 9082. (d) Sun, Z. H.; Yang, Z.; Zhou, J.; Yeung, M. H.; Ni, W.; Wu, H.; Wang, J. F. *Angew. Chem., Int. Ed.* **2009**, *48*, 2881. (e) Ni, W. H.; Kou, X. S.; Yang, Z.; Wang, J. F. *ACS Nano* **2008**, *2*, 677.

(12) (a) Yang, X. M.; Tryk, D. A.; Hasimoto, K.; Fujishima, A. *Appl. Phys. Lett.* **1996**, *69*, 4020. (b) Rosario-Castro, B. I.; Fachini, E. R.; Hernández, J.; Pérez-Davis, M. E.; Cabrera, C. R. *Langmuir* **2006**, *22*, 6102. (c) Silien, C.; Dreesen, L.; Cecchet, F.; Thiry, P. A.; Peremans, A. *J. Phys. Chem. C* **2007**, *111*, 6357.

(13) (a) Wang, Z. L.; Mohamed, M. B.; Link, S.; El-Sayed, M. A. *Surf. Sci.* **1999**, *440*, L809. (b) Liu, M.; Guyot-Sionnest, P. *J. Phys. Chem. B* **2005**, *109*, 22192. (c) Keul, H. A.; Moller, M.; Bockstaller, M. R. *Langmuir* **2007**, *23*, 10307. (d) Carbo-Argibay, E.; Rodriguez-Gonzalez, B.; Pacifico, J.; Pastoriza-Santos, I.; Perez-Juste, J.; Liz-Marzan, L. M. *Angew. Chem., Int. Ed.* **2007**, *46*, 8983.

(14) (a) Katz-Boon, H.; Rossouw, C. J.; Weyland, M.; Funston, A. M.; Mulvaney, P.; Etheridge, J. *Nano Lett.* **2011**, *11*, 273. (b) Carbó-Argibay, E.; Rodríguez-González, B.; Gómez-Graña, S.; Guerrero-Martínez, A.; Pastoriza-Santos, I.; Pérez-Juste, J.; Liz-Marzán, L. M. *Angew. Chem., Int. Ed.* **2010**, *49*, 9397.

(15) (a) Zhang, K.; Xiang, Y.; Wu, X.; Feng, L.; He, W.; Liu, J.; Zhou, W.; Xie, S. *Langmuir* **2009**, *25*, 1162. (b) Chen, H. J.; Wang, F.; Li, K.; Woo, K. C.; Wang, J. F.; Li, Q.; Sun, L. D.; Zhang, X. X.; Lin, H. Q.; Yan, C. H. *ACS Nano* **2012**, *6*, 7162.
(16) Zhang, W.; Gallinet, B.; Martin, O. *Phys. Rev. B* **2010**, *81*, 233407.
(17) (a) Dreaden, E. C.; Near, R. D.; Abdallah, T.; Talaat, M. H.; El-Sayed, M. A. *Appl. Phys. Lett.* **2011**, *98*, 183115. (b) Zhang, S. P.; Xu, H. X. *ACS Nano* **2012**, *6*, 8128.
(18) Chu, M. W.; Myroshnychenko, V.; Chen, C. H.; Deng, J. P.; Mou, C. Y.; de Abajo, F. J. G. *Nano Lett.* **2009**, *9*, 399.
(19) (a) Feng, Y. H.; Wang, Y.; Wang, H.; Chen, T.; Tay, Y. Y.; Yao, L.; Yan, Q. Y.; Li, S. Z.; Chen, H. Y. *Small* **2012**, *8*, 246. (b) Chen, T.; Wang, H.; Chen, G.; Wang, Y.; Feng, Y. H.; Teo, W. S.; Wu, T.; Chen, H. Y. *ACS Nano* **2010**, *4*, 3087. (c) Chen, G.; Wang, Y.; Yang, M. X.; Xu, J.; Goh, S. J.; Pan, M.; Chen, H. Y. *J. Am. Chem. Soc.* **2010**, *132*, 3644.
(20) Funston, A. M.; Novo, C.; Davis, T. J.; Mulvaney, P. *Nano Lett.* **2009**, *9*, 1651.
(21) Huang, Y. F.; Zhu, H. P.; Liu, G. K.; Wu, D. Y.; Ren, B.; Tian, Z. Q. *J. Am. Chem. Soc.* **2010**, *132*, 9244.
(22) Gdowski, G. E.; Felter, T. E.; Stulen, R. H. *Surf. Sci.* **1987**, *181*, L147.
(23) Huang, J. F.; Vongehr, S.; Tang, S. C.; Lu, H. M.; Meng, X. K. *J. Phys. Chem. C* **2010**, *114*, 15005.
(24) (a) Dong, B.; Fang, Y. R.; Chen, X. W.; Xu, H. X.; Sun, M. T. *Langmuir* **2011**, *27*, 10677. (b) Sun, M. T.; Zhang, Z. L.; Zheng, H. R.; Xu, H. X. *Sci. Rep.* **2012**, *2*, 647. (c) Xie, W.; Walkenfort, B.; Schlücker, S. *J. Am. Chem. Soc.* **2013**, *135*, 1657.
(25) Joseph, V.; Engelbrekt, C.; Zhang, J. D.; Gernert, U.; Ulstrup, J.; Kneipp, J. *Angew. Chem., Int. Ed.* **2012**, *51*, 7592.
(26) Nahm, T. U.; Jung, R.; Kim, J. Y.; Park, W. G.; Oh, S. J.; Park, J. H.; Allen, J.; Chung, S. M.; Lee, Y.; Whang, C. *Phys. Rev. B* **1998**, *58*, 9817.
(27) Nutt, M. O.; Hughes, J. B.; Wong, M. S. *Environ. Sci. Technol.* **2005**, *39*, 1346.